



Ruthenium nanofibers as efficient counter electrodes for dye-sensitized solar cells



Geon-Hyoung An^a, HyeLan An^b, Hyo-Jin Ahn^{a,b,*}

^a Program of Materials Science & Engineering, Convergence Institute of Biomedical Engineering and Biomaterials, Seoul National University of Science and Technology, Seoul 139-743, Korea

^b Department of Materials Science and Engineering, Seoul National University of Science and Technology, Seoul 139-743, Korea

ARTICLE INFO

Article history:

Received 10 May 2016

Received in revised form 14 June 2016

Accepted 17 June 2016

Available online 18 June 2016

Keywords:

Dye-sensitized solar cells

Counter electrode

Electrocatalytic activity

Ruthenium

ABSTRACT

The counter electrode has a strong influence on the photovoltaic performance of dye-sensitized solar cells (DSSCs). Thus, we introduce a novel approach where Ru nanofibers consisting of nano-sized grains are used instead of the typical Pt counter electrodes for DSSCs. The Ru nanofibers can be successfully prepared via electrospinning followed by post-calcination and hydrogen reduction. This sequential approach provides a novel nanoarchitecture. This architecture consists of nano-sized grains and a unique network structure, which affords high electrical conductivity. The resultant Ru nanofibers exhibit properties of improved photovoltaic performance: (I) lower charge transfer resistance ($12.5 \Omega \text{ cm}^{-2}$), (II) higher short-circuit current density (14.77 mA cm^{-2}), and (III) higher photovoltaic conversion efficiency (6.23%), which is comparable to a commercial Pt counter electrode. The improved photovoltaic performance of the counter electrode in the DSSC is attributed to the combined effects of small grain size which results in a high number of electrochemical sites, high electrical conductivity that leads to improved electrocatalytic activity, and a unique network structure that allows for rapid electron transfer and rapid diffusion of the electrolyte.

© 2016 Elsevier B.V. All rights reserved.

1. Introduction

Since the first report in 1991, dye-sensitized solar cells (DSSCs) have been one of the more anticipated alternatives to the conventional silicon solar cells due to their low cost, relatively high solar conversion efficiency, easy fabrication, and eco-friendly nature [1–5]. In general, DSSCs are composed of a large-band-gap n-type semiconductor that serves as the working electrode, dye molecules that serve as the sensitizer, an iodide/triiodide (I_3^-/I^-) redox-coupled electrolyte and catalysts that serve as the counter electrode [6–8]. The recent research and development of DSSCs has mainly focused on the improvement of their solar conversion efficiency. Among these improvements, the counter electrode performs as the catalyst by reducing the redox species after electron injection and thereby regenerates the dye molecules [9,10]. Therefore, the ideal counter electrode in DSSCs should have a large number of electrochemical active sites, a low charge transfer resistance, and electrochemical stability [9–12]. Currently, Pt is typically used as the counter electrode because of its excellent electrocatalytic activity and high electrical

conductivity [9]. However, Pt is very expensive and has limited availability [10]. Therefore, there is a desperate need to find an efficient alternative for Pt as the counter electrode material in DSSCs.

In recent years, the carbonaceous materials (activated carbon, carbon black, carbon nanotube, carbon nanofiber, and graphene), conducting polymers (PEDOT, PEDOT:PSS, PANI, and Ppy), transition metals (Co and Ni), metal and metalloid oxides (Al_2O_3 , SnO_2 , SiO_2 , and Ga_2O_3), metal sulfides (Co_9S_8 , FeS_2 , SnS_2 , and NiS_2), metal carbides (TiC, Cr_3C_2 , and VC) and metal nitrides (TiN, VN, and ZrN) have been used as counter electrodes in DSSCs [9–14]. Among them, the transition metals are the most promising choice for the use as the counter electrode due to their rapid redox reactions which owe to their high electrical conductivity [15–17]. However, it is noted that only a few transition metals have been explored as the counter electrode of DSSCs. Among the transition metals, Ru is an attractive material for the counter electrode of DSSCs due to its high electrical conductivity, high electrocatalytic activity, and excellent electrochemical stability over a wide potential range [15–17]. In addition, the cost of Ru is much less than Pt. In addition to cost and electrochemical properties, another important characteristic of an ideal catalyst is its network structure. It is well known that a network structure consisting of one-dimensional nanofibers can provide efficient electron transfer and a rapid diffusion rate of the electrolyte, both of which are responsible for high-efficiency in DSSCs [18–21]. However, the use of Ru nanofibers, which can be

* Corresponding author at: Program of Materials Science & Engineering, Convergence Institute of Biomedical Engineering and Biomaterials, Seoul National University of Science and Technology, Seoul 139-743, Korea.

E-mail address: hjahn@seoultech.ac.kr (H.-J. Ahn).

fabricated by electrospinning, post-calcination, and hydrogen reduction in series, has not yet been studied.

Therefore, we synthesized Ru nanofibers as an alternative to commercial Pt in DSSCs using a sequential process of electrospinning, post-calcination, and hydrogen reduction. This unique strategy allowed for the fabrication of a counter electrode with high electrical conductivity which exhibits higher solar conversion efficiency with excellent electrocatalytic activity compared to commercial Pt. These results indicate that the Ru nanofibers have great potential for being the counter electrode material for high-efficiency DSSCs.

2. Material and methods

2.1. Chemicals

Polyacrylonitrile (PAN, $M_w = 150,000$ amu), Ru(III) chloride hydrate ($\text{RuCl}_3 \cdot x\text{H}_2\text{O}$), *N,N*-dimethylformamide (DMF, 99.8%), and *N*-methyl-2-pyrrolidinone (NMP, 99.5%) were purchased from Sigma-Aldrich. All chemicals were used without further purification.

2.2. Synthesis of Ru nanofibers consisting of nano-sized grains

Ru nanofibers consisting of nano-sized grains were synthesized using electrospinning, post-calcination, and hydrogen reduction in sequence. Additionally, carbon nanofibers embedded with Ru nanoparticles and RuO_2 -and-Ru nanofiber composites were also synthesized by omitting the post-calcination and reduction step and just the reduction step, respectively. First, 10 wt% PAN and 3 wt% $\text{RuCl}_3 \cdot x\text{H}_2\text{O}$ were dissolved in DMF with vigorous stirring for 5 h to obtain the carbon nanofibers embedded with Ru nanoparticles. For electrospinning, the feeding rate and the voltage were maintained at 0.03 mL h^{-1} and $\sim 13 \text{ kV}$, respectively. The distance between the collector and a 23-gauge needle was set at 15 cm under 10% humidity in the chamber. The as-spun nanofibers were stabilized at 280°C for 2 h in air and then carbonized at 800°C for 2 h under a nitrogen atmosphere. In order to remove the CNF matrix, the Ru nanoparticles-embedded carbon nanofibers were calcined in air using a box furnace at 400°C for 30 min. As a result, RuO_2 -and-Ru nanofiber composites were obtained. Then, the hydrogen reduction was carried out to synthesize the Ru nanofibers consisting of nano-sized grains. We thus synthesized three types of the samples: Ru nanoparticles-embedded carbon nanofibers, RuO_2 -and-Ru nanofiber composites, and the Ru nanofibers.

2.3. Characterization

The morphologies and structures of the nanofibers were investigated by field-emission scanning electron microscopy (FESEM; S-4800, Hitachi) and transmission electron microscopy (MULTI/TEM; Tecnai G², KBSI Gwangju Center). The crystal structures and chemical bonding states of the samples were observed using X-ray diffractometry (XRD; D/Max 2500 V, Rigaku) with $\text{CuK}\alpha$ radiation in the 2θ range of 10° – 90° at a step size of 0.02° and X-ray photoelectron spectroscopy (XPS; ESCALAB 250, Thermo scientific) with an $\text{AlK}\alpha$ X-ray source. The XPS spectra were standardized to the C1s core level (284.5 eV).

2.4. Electrochemical characterization

The prepared samples were applied as a counter electrode for DSSCs. Pastes for the counter electrodes, which were made up of each of the resultant samples, ketjen black (KJB, Alfa Aesar), and polyvinylidene difluoride (PVDF, Alfa Aesar) at a ratio of 7:2:1 in *N*-methyl-2-pyrrolidinone (NMP, Samchun), were prepared. The PVDF in the counter electrode could innovatively increase the adhesion between the Ru nanofibers and the FTO glass, leading to the improved physical stability of the counter electrode in DSSCs. [6,9,10]. The pastes were then squeeze-printed onto fluorine-doped SnO_2 glass (FTO, $8 \Omega/\text{square}$,

Pilkington) and then dried at 100°C for 12 h. For comparison, the commercial Pt counter electrode was prepared from a solution containing chloroplatinic acid hydrate ($\text{H}_2\text{PtCl}_6 \cdot x\text{H}_2\text{O}$, Aldrich) and 2-propanol via spin coating and then annealed at 450°C for 0.5 h. For fabrication of a working electrode, the TiO_2 paste was formed by mixing TiO_2 (P25, Degussa AG), hydroxypropyl cellulose (HPC, $M_w \sim 80,000 \text{ g mol}^{-1}$, Aldrich), and acetyl acetone (Aldrich) in DI water. The well-dispersed pastes were coated by the squeeze-printing process and subsequently annealed at 500°C for 1 h. After cooling, the electrode was soaked in 0.5 M solution of N719 dye (Ru-535-bisTBA, Solaronix) in ethanol for 24 h and washed with ethanol to remove the excess dye which had not been physically adsorbed. Finally, sandwich-type cells were assembled with the prepared working and counter electrode and then injected with a liquid electrolyte composed of 1-butyl-3-methylimidazolium iodide (BMII, Aldrich), iodine (I_2 , Merck KGaA), guanidine thiocyanate (GuSCN, Aldrich), and 4-*tert*-butylpyridine (4TBP, Aldrich) in acetonitrile/valeronitrile (85:15 (v/v)). The catalytic activity was performed using cyclic voltammetry (CV) with a conventional three-electrode system at a scan rate of 50 mV s^{-1} from -0.3 to 1.1 V . An electrolyte containing 10 mM LiI (Lithium iodide, Aldrich), 1 mM I_2 (Iodine, Merck), and 0.1 M LiClO_4 (Lithium perchlorate, Aldrich) in acetonitrile was used. Electrochemical impedance spectra (EIS) was investigated using potentiostat/galvanostat (Ecochemie Autolab, PGST302N) under amplitude of 10 mV s^{-1} in the frequency range from 0.05 to 100 kHz. A solar simulator (PEC L01 with 150 W Xenon Arc Lamp, Peccell) was used to evaluate the current density-voltage (J-V) characteristics under AM 1.5G irradiation (ca. 100 mA cm^{-2}).

3. Results and discussion

Fig. 1a–c show FESEM images of Ru nanoparticles-embedded carbon nanofibers, RuO_2 -and-Ru nanofiber composites, and the Ru nanofibers. All samples exhibited an interconnected network structure composed of the one-dimensional nanofibers. This structure can thus provide a rapid electron transfer and a rapid diffusion rate of electrolyte during the photovoltaic process, which results in a high photovoltaic conversion efficiency [18–21]. As shown in Fig. 1a, the FESEM images of the Ru nanoparticles-embedded carbon nanofibers showed smooth

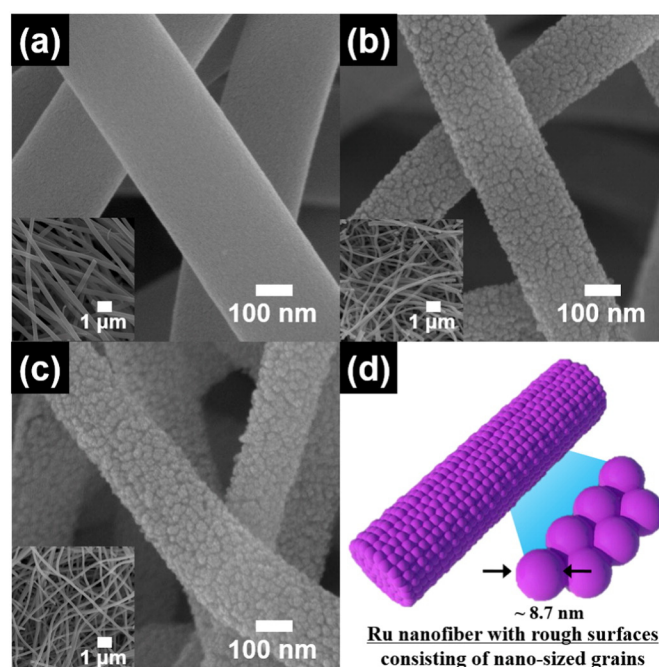


Fig. 1. FESEM images and inserted FESEM images of (a) carbon nanofibers embedded with Ru nanoparticles, (b) RuO_2 -and-Ru nanofiber composites, and (c) Ru nanofibers. (d) A schematic illustration of the Ru nanofibers.

surfaces and uniform morphology without any beads on the nanofiber surface, which means the Ru nanoparticles were wholly embedded within the CNF matrix. Also, the diameter of Ru nanoparticles-embedded carbon nanofibers was estimated to be 317–343 nm. The FESEM images of the RuO₂-and-Ru nanofiber composites (Fig. 1b) and Ru nanofibers (Fig. 1c) showed rough surfaces consisting of nano-sized grains with reduced diameters in the range of 181–211 nm for RuO₂-and-Ru nanofiber composites (Fig. 1b), and 183–209 nm for Ru nanofibers (Fig. 1c). These results are ascribed to an exhaustion of CNF matrix after post-calcination by an oxidation reaction between carbon and oxygen. Fig. 1d shows a schematic of the Ru nanofibers, which indicates that the unique one-dimensional nanofiber with rough surfaces consisting of nano-sized grains of Ru is ideal for high-performance DSSCs. This is the ideal structure because the one-dimensional nanofibers can directly guide high-efficiency DSSCs due to efficient electron transfer and a rapid diffusion rate of the electrolyte during the photovoltaic process.

To further examine the nanostructure of the samples, TEM studies were carried out. Fig. 2 shows low-resolution (Fig. 2a–c) TEM images of Ru nanoparticles-embedded carbon nanofibers, the RuO₂-and-Ru nanofiber composites, and the Ru nanofibers and Fig. 2d shows the high-resolution TEM image of the Ru nanofibers. The dark spots in the Ru nanoparticles-embedded carbon nanofibers (Fig. 2a) are well-distributed Ru nanoparticles, which are 1–2 nm in size, inside the CNF matrix. After post-calcination, the RuO₂-and-Ru nanofiber composites (Fig. 2b) showed rough surfaces consisting of nano-sized grains (7–9 nm) not embedded within the CNF matrix. The formation of rough surfaces consisting of nano-sized grains could be explained by the exhaustion of CNF matrix and grain growth of Ru induced by Ostwald ripening processes during post-calcination due to the presence of oxygen [22]. Thus, we observed noticeable morphological changes at the surface of the nanofibers, which led to the formation of porous structures after post-calcination. After hydrogen reduction, the morphology of the Ru nanofibers (Fig. 2c and d) exhibited the roughness similar to that of the RuO₂-and-Ru nanofiber composites without any morphological changes. The only phase change that occurs is the reduction from RuO₂ to Ru. Therefore, Ru nanofibers with rough surfaces consisting of nano-sized grains were successfully obtained. This unique architecture of Ru nanofibers

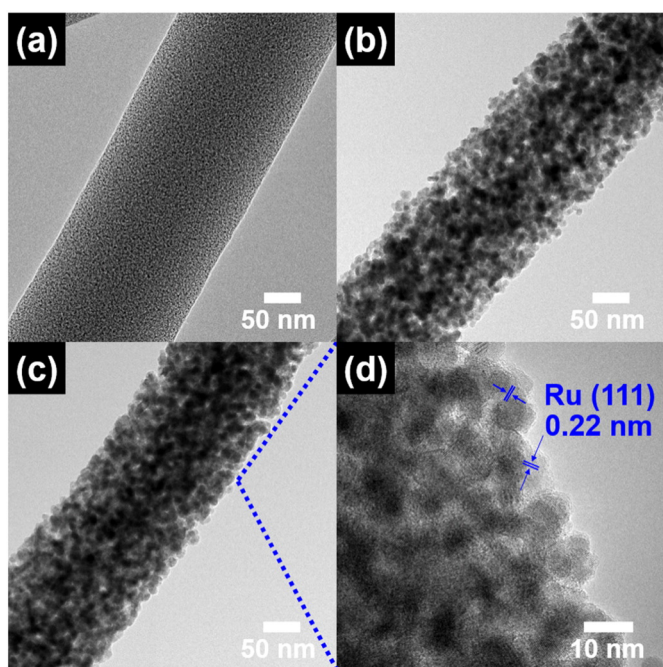


Fig. 2. Low-resolution TEM images of (a) carbon nanofibers embedded with Ru nanoparticles, (b) RuO₂-and-Ru nanofiber composites, and (c) Ru nanofibers. (d) High-resolution TEM images of Ru nanofibers.

with nano-sized grains can effectively provide high electrochemical active sites, resulting in high-performance DSSCs.

Fig. 3a shows the XRD patterns of the Ru nanoparticles-embedded carbon nanofibers, the RuO₂-and-Ru nanofiber composites, and the Ru nanofibers. The Ru nanoparticles-embedded carbon nanofibers displayed broad peaks at around 25° corresponding to the (002) layers of graphite and diffraction peaks at 44.0° corresponding to the (101) plane of Ru with a hexagonal structure (space group *P6₃/mmc*[194]) (JCPDS card No. 06-0663). The low intensity of the diffraction peaks of the Ru phases in Ru nanoparticles-embedded carbon nanofibers are due to the ultra-small Ru nanoparticles (1–2 nm), which is in good agreement with the TEM results. The RuO₂-and-Ru nanofiber composites showed the mixed phases consisting of RuO₂ phases and Ru phases because of an oxidation ambience during post-calcination. The diffraction peaks of RuO₂-and-Ru nanofiber composites were observed at 28.0°, 35.1°, and 54.3° corresponding to the (110), (101), and (211) planes of RuO₂ phases with a tetragonal structure (space group *P4₂/mmm*[136]) (JCPDS card No. 88-0322). The other diffraction peaks of RuO₂-and-Ru nanofiber composites were observed at 44.0° corresponding to the (101) plane of Ru the phases. The diffraction peaks of the Ru nanofibers were observed at 38.4°, 42.1°, 44.0°, and 58.3° corresponding to the (100), (002), (101), and (102) planes of only the Ru phases, which implies that RuO₂ was successfully reduced to Ru during the hydrogen reduction step.

In order to further investigate the grain sizes of the RuO₂-and-Ru nanofiber composites and the Ru nanofibers, the diffraction peaks were calculated using the Scherrer equation given below in which λ is the X-ray wavelength, β is the full width at half maximum (FWHM), and θ is the Bragg angle [23–25].

$$D = 0.9\lambda / (\beta \cos\theta)$$

The average size of the RuO₂-and-Ru nanofiber composites was calculated using (110), (101), and (211) planes and was ~8.5 nm. The average size of the Ru nanofibers was likewise obtained using (100), (002), and (101) planes and was ~8.7 nm, which is in good agreement with the TEM results. Thus, the XRD results indicate that the hydrogen reduction can efficiently provide the desired phase change from RuO₂-to-Ru without any noticeable morphological change. To investigate the chemical bonding states, XPS measurements were carried out. As shown in Fig. 3b–d, the XPS of the Ru-3p core levels of Ru nanoparticles-embedded carbon nanofibers, the RuO₂-and-Ru nanofiber composites, and the Ru nanofibers showed that the Ru-3p_{3/2} and Ru-3p_{1/2} photoelectrons are observed at ~462.0 eV and ~484.6 eV, corresponding to the metallic Ru phases [26,27]. The XPS of the Ru-3p core levels of the RuO₂-and-Ru nanofiber composites (Fig. 3c), and the Ru nanofibers (Fig. 3d) exhibited two different signals at ~464.6 and ~487.6 eV, which correspond to the Ru-3p_{3/2} and Ru-3p_{1/2} photoelectrons of the RuO₂ phase [28]. The percentage of the Ru phase of the RuO₂-and-Ru nanofiber composites and the Ru nanofibers was 69% and 96%, respectively, implying that the hydrogen reduction was successful. Nevertheless, the Ru nanofibers still showed small amounts of the RuO₂ phase which can be attributed to the oxidation reactions of Ru with O₂ and water vapor in the air. Based on XRD and XPS results, the increased amount of the metallic Ru phases in the Ru nanofibers can directly improve the electrical conductivity, leading to an increased performance due to a low charge transfer resistance in DSSCs.

To examine the electrocatalytic activity in the I₃⁻/I⁻ electrochemical system, cyclic voltammetry (CV) was performed using a three-electrode system. As shown in Fig. 4a, all samples showed two pairs of redox peaks, corresponding to the following reactions: I₃⁻ + 2e⁻ ↔ 3I⁻ (left) and 3I₂ + 2e⁻ ↔ 2I₃⁻ (right). The electrochemical reaction of I₃⁻/I⁻ in the low potential range is the focus of our analysis. The high peak current density and the small peak-to-peak separation (E_{pp}) between the redox peaks denote a small over-potential and a high electrocatalytic activity toward the I₃⁻/I⁻ redox reduction in the counter

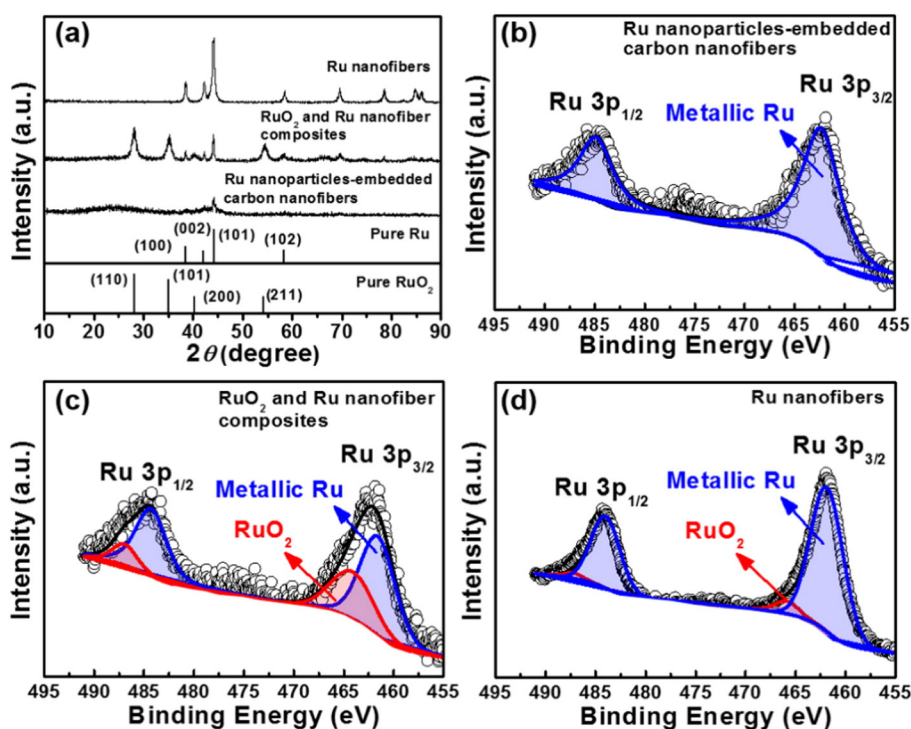


Fig. 3. (a) XRD patterns of carbon nanofibers embedded with Ru nanoparticles, RuO₂-and-Ru nanofiber composites, and Ru nanofibers. XPS spectra of Ru-3p of (b) carbon nanofibers embedded with Ru nanoparticles, (c) RuO₂-and-Ru nanofiber composites, and (d) Ru nanofibers.

electrode [29–31]. The Ru nanofibers exhibited higher peak current density ($\sim 6.3 \text{ mA cm}^{-2}$) and smaller E_{pp} ($\sim 2.53 \text{ V}$) compared to the commercial Pt ($\sim 6.1 \text{ mA cm}^{-2}$, $\sim 2.75 \text{ V}$), Ru nanoparticles-embedded carbon nanofibers ($\sim 5.8 \text{ mA cm}^{-2}$, $\sim 3.33 \text{ V}$), and the RuO₂-and-Ru nanofiber composites ($\sim 6.0 \text{ mA cm}^{-2}$, $\sim 2.73 \text{ V}$). The higher peak current density and smaller E_{pp} of the Ru nanofibers results in an enhancement in its electrocatalytic activity to promote regeneration of the dye. The increased peak current density can be attributed to the nanofibers' rough surface while the smaller E_{pp} can be attributed to the increased electrical conductivity of the Ru nanofibers. To further confirm the electrochemical impedance on the counter electrode, EIS measurements were performed using symmetric cell configurations. The obtained Nyquist plots are shown in Fig. 4b. In the Nyquist plot, the intercept on the real axis at the high frequency region offers the series resistance (R_s), which describes the interfacial resistance of the ohmic contact between the counter electrode and the FTO glass substrate [32–34]. The semicircle in the high frequency region represents the charge transfer

resistance (R_{ct}) at the interface of the counter electrode which determines electrocatalytic activity of the counter electrode toward I_3^- reduction [32–34]. Signals in the low-frequency range represent the Warburg diffusion resistance of the I_3^-/I^- redox couple in the electrolyte [30]. The R_s values of all the samples were almost identical ($\sim 13.9 \Omega \text{ cm}^{-2}$), indicating that the counter electrodes are successfully prepared and are very compatible with FTO glass substrates. The R_{ct} value of the commercial Pt, Ru nanoparticles-embedded carbon nanofibers, the RuO₂-and-Ru nanofiber composites, and the Ru nanofibers are 16.4, 26.8, 20.3, and $12.5 \Omega \text{ cm}^{-2}$, respectively. Noticeably, Ru nanofibers showed the lowest R_{ct} value, which is consistent with the improved electrocatalytic activity with a rapid rate for I_3^- reduction due to the higher electrical conductivity of metallic Ru phases versus those of the RuO₂. This is in good agreement with the CV results. Moreover, the poor performance of the Ru nanoparticles-embedded carbon nanofibers may be attributed to the fact that the Ru nanoparticles are encapsulated within the CNF matrix, which results in the low electrocatalytic activity and a large

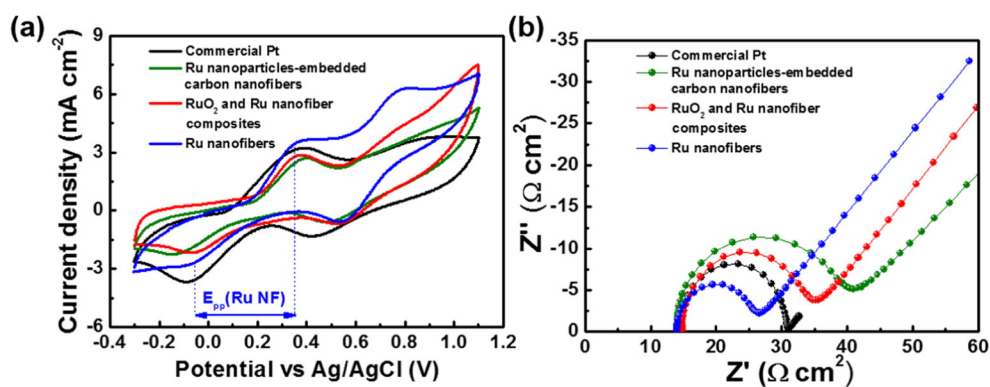


Fig. 4. (a) Cyclic voltammograms of commercial Pt, carbon nanofibers embedded with Ru nanoparticles, RuO₂-and-Ru nanofiber composites, and Ru nanofibers in I_3^-/I^- electrolyte composed of 10 mM LiI, 1 mM I₂, and 0.1 M LiClO₄ in acetonitrile at a scan rate of 50 mV s^{-1} . (b) Nyquist plots of symmetric cell configurations under amplitude of 10 mV s^{-1} in the frequency range from 0.05 to 100 kHz.

R_{ct} . Thus, both the CV and EIS results are consistent and suggest that the Ru nanofibers perform well as the counter electrode for high-performance DSSCs.

The photocurrent density–voltage (J–V) curves of commercial Pt, the Ru nanoparticles–embedded carbon nanofibers, the RuO₂-and-Ru nanofiber composites, and the Ru nanofibers for DSSCs were evaluated under a simulated AM 1.5G illumination intensity of 100 mW cm⁻², as shown in Fig. 5. The fill factor (FF) and power conversion efficiency (η) of DSSCs were calculated from the J–V curve according to the following equations where V_{max} and J_{max} are the voltage and current density at the point of maximum power in the J–V curves, V_{oc} is the open-circuit voltage, J_{sc} is the short-circuit current density (mA cm⁻²), and P_{in} is the incident light power (100 mW cm⁻²) [30,35,36].

$$FF = \frac{V_{max} \times J_{max}}{V_{oc} \times J_{sc}}$$

$$\eta(\%) = \frac{V_{oc} \times J_{sc} \times FF}{P_{in}} \times 100\%$$

The detailed photovoltaic parameters are listed in Table 1. The J_{sc} values of the RuO₂-and-Ru nanofiber composites and the Ru nanofibers were increased after post-calcination compared to those of the Ru nanoparticles–embedded carbon nanofibers, indicating that Ru and RuO₂ with rough surfaces consisting of nano-sized grains have a strong effect on the electro-catalytic activity. In addition, the J_{sc} value of the Ru nanofibers (14.77 mA cm⁻²) was higher than the RuO₂-and-Ru nanofiber composites because of an increased electrical conductivity. Additionally, the η of the Ru nanofibers was 6.23%, which is higher than that of commercial Pt (6.04%) and the other counter electrodes studied. The improved η of the Ru nanofibers could be attributed to the higher J_{sc} values as well as the lower R_{ct} values, which is also supported by the EIS results. Thus, the excellent electrochemical performance of the Ru nanofibers as the counter electrode for DSSCs can be attributed to three main causes: (I) the Ru nanofibers with rough surfaces consisting of nano-sized grains results in a high number of electrochemical sites, leading to increased contact area between the electrode and the electrolyte, (II) the metallic Ru phase can directly provide the increased electrical conductivity related to a rapid rate for I₃⁻ reduction, leading to lower R_{ct} values and higher J_{sc} values as well as higher η , and (III) the unique network structures composed of the one-dimensional NFs can always provide a rapid electron transfer and a rapid diffusion rate of electrolyte during the photovoltaic process, resulting in lower Warburg diffusion resistance.

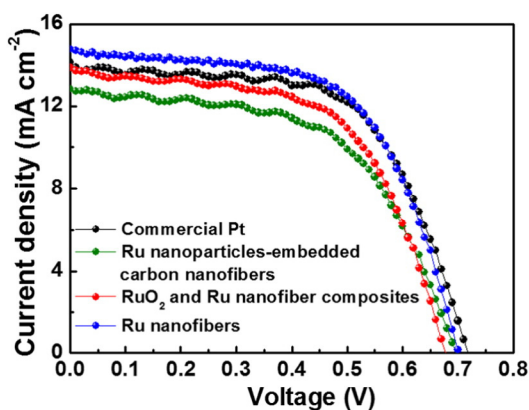


Fig. 5. The photocurrent density–voltage curves of commercial Pt, carbon nanofibers embedded with Ru nanoparticles, RuO₂-and-Ru nanofiber composites, and Ru nanofibers for DSSCs.

Table 1

Parameter summary of photovoltaic performance for commercial Pt, carbon nanofibers embedded with Ru nanoparticles, RuO₂-and-Ru nanofiber composites, and Ru nanofibers as counter electrode for DSSCs.

Electrodes	V_{oc} (V)	J_{sc} (mA cm ⁻²)	FF (%)	η (%)
Commercial Pt	0.71	14.13	60.25	6.04
Ru nanoparticles-embedded carbon nanofibers	0.69	12.84	56.20	4.97
RuO ₂ and Ru nanofiber composites	0.69	13.65	60.13	5.66
Ru nanofibers	0.70	14.77	60.26	6.23

4. Conclusions

Ru nanofibers were synthesized using a sequential process of electrospinning, post-calcination, and hydrogen reduction. The Ru nanofibers exhibited rough surfaces consisting of nano-sized grains as well as a unique network structure. The synthesized Ru nanofibers showed improved photovoltaic performance, including the lowest R_{ct} values (12.5 Ω cm⁻²), the highest J_{sc} values (14.77 mA cm⁻²), and the highest η (6.23%) among all the samples tested. The improved photovoltaic performance of the Ru nanofibers can be explained by three main aspects: (I) the rough surfaces consisting of nano-sized grains results in a high number of electrochemical sites between the electrode and the electrolyte, (II) the metallic Ru phase shows high electrical conductivity and improved electrocatalytic activity with a rapid rate for I₃⁻ reduction and (III) a unique network structure that allows for a rapid electron transfer and a rapid diffusion rate of electrolyte during the photovoltaic process. Therefore, the Ru nanofibers are a promising material for the use as efficient counter electrodes for high-performance DSSCs.

Acknowledgments

This work was supported by Grant No. 10046672 from the Ministry of Knowledge Economy (MKE) and R&D Program for Technology of Specialized Materials particularly designed for venture business funded by the Ministry of Knowledge Economy, Republic of Korea.

References

- [1] B. O'Regan, M. Graetzel, *Nature* 353 (1991) 737–740.
- [2] U. Bach, D. Lupo, P. Comte, J.E. Moser, F. Weissortel, J. Salbeck, H. Spreitzer, M. Graetzel, *Nature* 395 (1998) 583–585.
- [3] M. Graetzel, *Nature* 414 (2001) 338–344.
- [4] D.-Y. Chen, J.-Y. Kao, C.-Y. Hsu, C.-H. Tsai, *J. Electroanal. Chem.* 766 (2016) 1–7.
- [5] S. Sheehan, K.R. Thampi, D.P. Dowling, *J. Electroanal. Chem.* 725 (2014) 12–18.
- [6] M. Ye, X. Wen, M. Wang, J. Iocozzia, N. Zhang, C. Lin, Z. Lin, *Mater. Today* 18 (2014) 155–162.
- [7] W.-C. Chang, L.-Y. Lin, W.-C. Yu, *J. Electroanal. Chem.* 757 (2015) 159–166.
- [8] S.S. Kanmani, N. Rajamanickam, K. Ramachandran, *J. Electroanal. Chem.* 767 (2016) 174–181.
- [9] S. Yun, P.D. Lund, A. Hinsch, *Energy Environ. Sci.* 8 (2015) 3495–3514.
- [10] H.G. Shiraz, F.R. Astaraie, *J. Mater. Chem. A* 3 (2015) 20849–20862.
- [11] H.-J. Kim, J.-H. Kim, C.H.S.S.P. Kumar, D. Punnoose, S.-K. Kim, C.V.V.M. Gopi, S.S. Rao, *J. Electroanal. Chem.* 739 (2015) 20–27.
- [12] D. Punnoose, H.-J. Kim, S.S. Rao, C.H.S.S.P. Kumar, *J. Electroanal. Chem.* 750 (2015) 19–26.
- [13] J. Zheng, W. Zhou, Y. Ma, W. Cao, C. Wang, L. Guo, *Chem. Commun.* 51 (2015) 12863–12866.
- [14] J. Zheng, W. Zhou, Y. Ma, W. Cao, C. Wang, L. Guo, *Chem. Commun.* 51 (2015) 12863–12866.
- [15] D.-J. Yun, H. Ra, S.B. Jo, W. Maeng, S. Lee, S. Park, J.-W. Jang, K. Cho, S.-W. Rhee, *ACS Appl. Mater. Interfaces* 4 (2012) 4588–4594.
- [16] J. Seok, K.Y. Ryu, J.A. Lee, I. Jeong, N.-S. Lee, J.M. Baik, J.G. Kim, M.J. Ko, K. Kim, M.H. Kim, *Phys. Chem. Chem. Phys.* 17 (2015) 3004–3008.
- [17] H.M. Villullas, F.I. Mattos-Costa, L.O.S. Bulhoes, *J. Phys. Chem. B* 108 (2004) 12898–12903.
- [18] G.-H. An, B.-R. Koo, H.-J. Ahn, *Phys. Chem. Chem. Phys.* 18 (2016) 6587–6594.
- [19] G.-H. An, J.I. Sohn, H.-J. Ahn, *J. Mater. Chem. A* 4 (2016) 2049–2054.
- [20] M. Zhang, E. Uchaker, S. Hu, Q. Zhang, T. Wang, G. Cao, J. Li, *Nanoscale* 5 (2013) 12342–12349.
- [21] G.-H. An, H.-J. Ahn, *J. Power Sources* 272 (2014) 828–836.
- [22] A. Baldan, *J. Mater. Sci.* 37 (2002) 2171–2202.
- [23] G.-H. An, H.-J. Ahn, W.-K. Hong, *J. Power Sources* 274 (2015) 536–541.

- [24] G.-H. An, S.-J. Kim, K.-W. Park, H.-J. Ahn, *ECS Solid-State Lett.* 3 (2014) M21–M23.
- [25] G.-H. An, H.-J. Ahn, *ECS Solid-State Lett.* 3 (2014) M29–M32.
- [26] C. Bock, C. Paquet, M. Couillard, G.A. Botton, B.R. MacDougall, *J. Am. Chem. Soc.* 126 (2004) 8028–8037.
- [27] G.-H. An, H.-J. Ahn, *J. Electroanal. Chem.* 707 (2013) 74–77.
- [28] G.-H. An, H.-J. Ahn, *J. Electroanal. Chem.* 744 (2015) 32–36.
- [29] K. Lee, S. Cho, M. Kim, J. Kim, J. Ryu, K.-Y. Shin, J. Jang, *J. Mater. Chem. A* 3 (2015) 19018–19026.
- [30] J.T. Park, C.S. Lee, J.H. Kim, *Nanoscale* 7 (2015) 670–678.
- [31] M. Chen, L.-L. Shao, X. Qian, T.-Z. Ren, Z.-Y. Yuan, *J. Mater. Chem. C* 2 (2014) 10312–10321.
- [32] W. Wang, X. Pan, W. Liu, B. Zhang, H. Chen, X. Fang, J. Yao, S. Dai, *Chem. Commun.* 50 (2014) 2618–2620.
- [33] S. Wozny, K. Wang, W. Zhou, *J. Mater. Chem. A* 1 (2013) 15517–15523.
- [34] H. Wang, W. Wei, Y.H. Hu, *J. Mater. Chem. A* 1 (2013) 6622–6628.
- [35] K. Saranya, A. Subramania, N. Sivasankar, S. Mallick, *Mater. Res. Bull.* 75 (2016) 83–90.
- [36] H.-R. An, H.L. An, W.-B. Kim, H.-J. Ahn, *ECS Solid-State Lett.* 3 (2014) M33–M36.